A Journal of the Gesellschaft Deutscher Chemiker

Angewandte International Edition Chemie

GDCh

www.angewandte.org

Accepted Article

Title: Spiderweb-like metal-organic framework multifunctional foam

Authors: Chen Tan, Michelle Lee, Mohammad Arshadi, Morteza Azizi, and Alireza Abbaspourrad

To be cited as: *Angew. Chem. Int. Ed.* 10.1002/anie.201916211
Angew. Chem. 10.1002/ange.201916211

Link to VoR: http://dx.doi.org/10.1002/anie.201916211
http://dx.doi.org/10.1002/ange.201916211

WILEY-VCH

10.1002/anie.201916211

Spiderweb-Like Metal-Organic Framework Multifunctional Foam

Chen Tan, Michelle C. Lee[†], Mohammad Arshadi[†], Morteza Azizi, Alireza Abbaspourrad[*]

Department of Food Science, Cornell University, Stocking Hall, Ithaca NY 14853, USA

[†] These authors contributed equally to this work

* Corresponding author: alireza@cornell.edu; +1 607 255-2923

Abstract

Processing metal-organic-frameworks (MOFs) into hierarchical macroscopic materials can greatly extend their practical applications. However, current strategies suffer from severe aggregation of MOFs and limited tuning of the hierarchical porous network. Here, we report a controlled strategy that can simultaneously tune the MOF loading, composition, spatial distribution, and confinement within various bio-originated macroscopic supports, as well as control the accessibility, robustness, and formability of the support itself. Our methodology enables the good dispersion of individual MOF nanoparticles on a spiderweb-like network within each macrovoid even at high loadings (up to 86 wt%), ensuring the foam pores are highly accessible for excellent adsorption and catalytic capacity. Additionally, this approach allows the direct pre-incorporation of other functional components into the framework. Our strategy provides a general toolbox for precise control over the properties of both the hierarchical support and MOF, opening new possibilities to construct tunable multi-scale porous platforms with desired functionalities.

Keywords: metal-organic frameworks; high internal phase emulsion; foam; organic-inorganic hybrid composites; oil-water separation

Introduction

Although metal-organic frameworks (MOFs) have shown great potential in various fields,[1–5] the bulk powder or crystal form of MOFs severely restrict their processability and use. MOF pellets and extrudates can be made, which are easier to handle and apply. However, the extrusion process often diminishes the adsorption and catalytic capacities of the MOFs due to the pore blockage of the resulting material, which has the added disadvantage of low mechanical stability.[6] As a result, new approaches and hierarchical macroscopic materials are needed to enhance the formability, mass loading, and performance of MOFs.

To date, the synthetic strategies toward this aim include: (i) forming mixed matrix membranes by doping pre-synthesized MOFs;[1,7,8] (ii) forming metal-organic gels through sol-gel processes;[9–11] and (iii) employing 2D/3D structured supports for loading MOF particles.[12–15] However, these approaches lack control over the organization of the MOFs inside the support, resulting in severe MOF aggregation, low MOF contents (usually < 30%), ill-defined hierarchical porosity, and poor formability of the support. Recently, researchers have further explored strategy (iii) through the introduction of flexible polymeric supports, achieving a few promising MOF aerogels and foams with desired mechanical properties and high MOF loading contents (e.g., 50–81%).[16–18] However, the aggregation of MOFs is inevitable if directly incorporating the pre-synthesized MOFs into the support. This aggregation problem can be reduced through *in situ* MOF growth,[19–21] but controlling the nucleation process remains challenging, as the initially grown MOF layer on the template surface prohibits the inward diffusion of precursors, preventing nucleation and growth. Moreover, current *in situ* MOF growth methods are often directly connected to the fabrication of the support,[21–23] which limits the ability to independently tune the material properties of each

component. Another challenge created by the limited tunability of these synthetic approaches is the difficulty in introducing additional functional components to the framework material.

To overcome these issues, in this work we demonstrate a new strategy that can readily control the loading, size, composition, spatial distribution, and confinement of MOFs within a hierarchically macroscopic biomaterial. The approach involves the *in situ* immobilization of MOFs on shell-cross-linked microspheres and subsequent centrifugation/freeze-drying to fabricate a foam derived from the high internal phase emulsion (HIPE) template. Our strategy relies on both the cross-linking of biomacromolecules to form microspheres that can confine the MOFs in a non-agglomerated fashion, and the independent synthesis of the MOFs and support to maximize the tunability of the material properties. For example, when using cellulose nanofibers (CNFs) and bovine serum albumin (BSA) as the cross-linking materials, we are able to engineer a well-defined meso-macroporous MOF foam composed of ordered macrovoids wherein abundant individual MOF nanoparticles can uniformly distribute on a spiderweb-like nanofibrous network. This unique 3D hierarchical architecture enables high MOF loading (up to 86 wt%) while maintaining good dispersion, high surface area, and accessibility for significant improvement of the MOF performance.

In sharp contrast to previous concepts of combining MOFs with HIPEs (see Table S1 for more details), this approach allows the separate preparation of the microspheres and HIPE template, as a result the MOF loading does not affect the formation of the HIPE, even at high contents. This eliminates the issues of poor HIPE stability (i.e., phase inversion induced by MOFs even at loading < 20 wt%), and non-uniform distribution. Additionally, this independent synthesis enables the direct incorporation of other functional components (e.g., hydrophobic polymers and metal/metal oxide nanomaterials) into the HIPE template, imparting additional functionalities to the MOFs.

We believe the strategy presented here provides a strong foundation for the future design of MOF multifunctional materials and tailored hierarchical architectures for various applications.

Results and Discussion

Synthesis of the MOF Foams. The synthesis of the MOF monolithic foam depends on (i) the formation of shell-cross-linked microspheres by acoustic cavitation, (ii) the *in situ* growth of MOF nanoparticles on the microspheres, and (iii) concentrating the MOF-microsphere composites to form stable HIPEs, which are then freeze-dried to produce the porous foam structure. For proof-of-concept, CNFs and BSA were chosen as the shell materials due to their numerous active groups (-SH, -NH_2, and -COOH) for both cross-linking and as biomineralization agents. Zeolitic imidazolate framework-8 (ZIF-8) was used as a model MOF in this system. In a typical experiment, we first use 2,2,6,6-tetramethylpiperidine-1-oxyl radical (TEMPO)-mediated oxidization method to exfoliate the CNFs from grape seed which is a waste material (~ 2–3 cents per kg) by the wine and grape juice industries.[24] 3-aminopropyltriethoxysilane (APTES) was then introduced to graft additional amine groups to these CNFs, which we confirmed by the appearance of new bands derived from the C-N stretching vibration in the attenuated total reflectance-Fourier transform infrared (ATR-FTIR) spectra (Figure S1). We expected that this modification would enhance the cross-linking degree of the CNFs with BSA. The APTES/TEMPO-treated grape seed showed a colloidally stable dispersion consisting of individualized CNFs with a uniform diameter of 3–4 nm and a few microns long (Figure 1a).

10.1002/anie.201916211

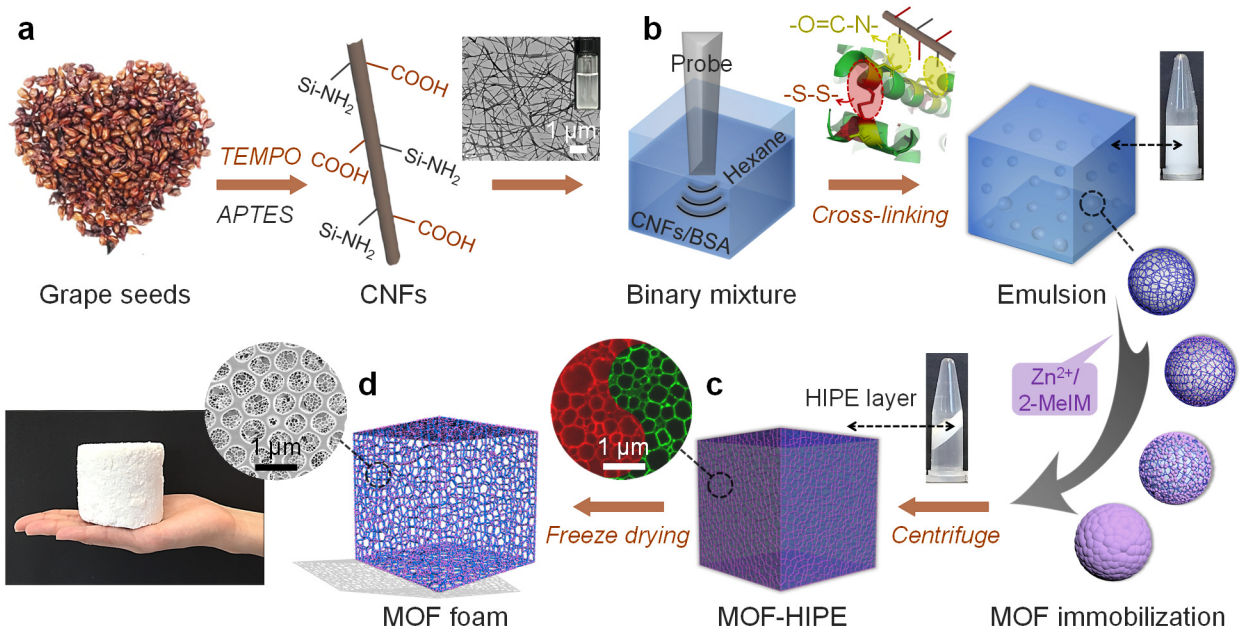

Figure 1. Schematic diagram of our strategy to design a spiderweb-like ZIF-8 monolithic foam. a) TEMPO-exfoliation of CNFs from grape seed with a further APTES modification. b) Fabrication of shell-cross-linked microspheres by ultrasonication using CNFs and BSA as the shell materials. Then, the precursor solutions, including zinc nitrate and 2-MeIM, were sequentially added to initiate the *in situ* growth of ZIF-8 at the microsphere surfaces. c) Following the centrifugation of the ZIF-8-immobilized microspheres at 2000 *g* for 5 min, a gel-like HIPE layer was collected. d) Freeze-drying to form the hierarchical porous ZIF-8 foam.

We then prepared a two-phase system, consisting of an oil phase (hexane) and an aqueous phase containing the CNFs and BSA (Figure 1b). By ultrasonicating this solution, the acoustic cavitation causes the CNFs and BSA at the oil-water interface to assemble into covalently shell-cross-linked microspheres enclosing an oil droplet—a process known as emulsion interfacial polymerization.[25] These cross-linked microspheres can then serve as templates for the *in situ* synthesis of MOFs by biomineralization. In this process, the MOF precursor solutions, including zinc nitrate and 2-methylimidazole (2-MeIM), were added dropwise into the microsphere suspension. We

anticipated the negatively charged microspheres would attract the Zn^{2+} ions, which could then coordinate with 2-MeIM and nucleate the growth of ZIF-8 nanoparticles. We then concentrated the resulting composite material by centrifugation, which excluded excess aqueous phase from the inter-microsphere volume to form a solid-like emulsion gel, i.e., HIPE featuring an internal phase volume fraction of ≥ 74% (Figure 1c). After evaporating both the water and oil phases of the HIPE by freeze-drying, we were able to obtain an ultralight, free-standing, and easily handled monolithic foam loaded with MOFs (Figure 1d).

Note, there are two key factors in this strategy that enable us to successfully synthesize a robust foam. One is the combination of CNFs and BSA as shell materials (Figure S2). Without the aid of BSA, the emulsion and subsequent HIPE template cannot be formed due to the lack of emulsifying ability of the CNFs. Similarly, though BSA alone can form a HIPE foam, it is loosely connected with poor stability under compression and stirring (Figure S3). In other words, the presence of the CNFs improves the mechanical strength of the foam. More interestingly, CNFs endow the foam with a spiderweb-like fibrous network within each void (Figure S4), which could provide more external surface and accelerate mass transfer. The other factor in the successful foam synthesis is the ultrasonication-induced formation of the CNF-BSA cross-linked shell, which ensured the excellent stability of the HIPEs in the high centrifugal field and corresponding foam during freeze-drying (Figure 1c-d). To demonstrate the stabilizing role of cross-linking, we prepared a conventional CNF-BSA emulsion by mechanically mixing using a homogenizer. However, this non-cross-linked emulsion exhibited poor stability, with severe phase separation after centrifugation under identical centrifugal conditions (Figure S5).

X-ray photoelectron spectroscopy (XPS) gave evidence for the types of cross-linking between the CNFs and BSA (Figure S6). For comparison, we studied the native BSA, sonicated BSA, and

10.1002/anie.201916211

sonicated CNF-BSA. The high-resolution N 1s spectra revealed that after native BSA was sonicated, the intensity of the peaks related to the bonds of amine (C-NH_2) at 397.5 eV and protonated amine (C-NH_3^+) at 401.6 eV became weaker, while the intensity of the amide bond (O=C-N) at 400.0 eV increased. At the same time, we saw an increase in the intensity of the -S-S- bond in the sonicated BSA, indicating the conversion of -SH to -S-S-.[26,27] These results suggested that ultrasonication induced interprotein cross-linking through the formation of amide linkages and disulfide bonds. When the native BSA was sonicated together with CNFs, the peaks of C-NH_2 and O=C-N further shifted to 397.6 eV and 399.9 eV, respectively. The high-energy component of the N 1s core-level spectra showed that the density of the amide bond also increased in the sonicated CNF-BSA. Thus, we believe that the amine sites in the CNFs also participated in cross-linking with the carboxylic sites of BSA. This conclusion was also supported by sodium dodecyl sulfate-polyacrylamide gel electrophoresis (SDS-PAGE) and ATR-FTIR analysis (Figure S7).

10.1002/anie.201916211

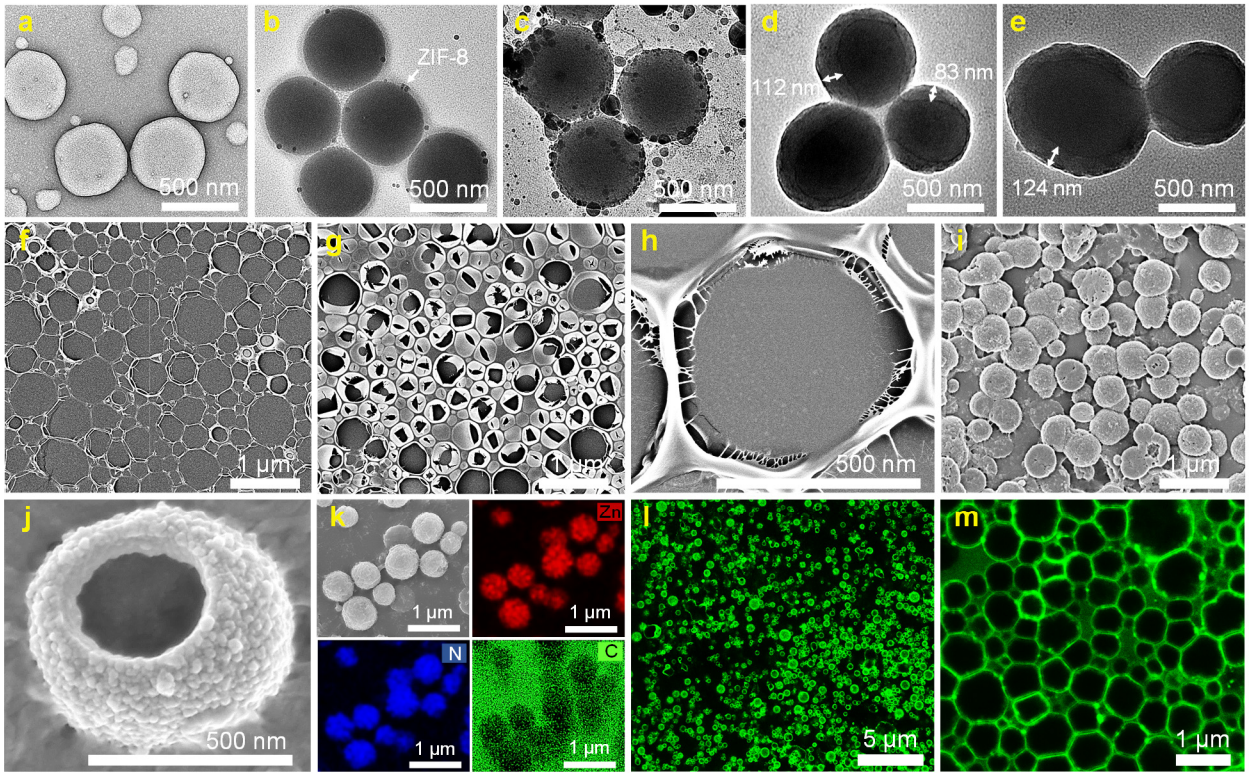

Figure 2. Immobilization of ZIF-8 on the shell cross-linked microspheres and the formation of the HIPEs. a-e) TEM images of the microspheres a) before and b-e) after the ZIF-8 biomineralization process at 2-MeIM concentrations of b) 40, c) 200, d) 400 mM, and e) 800 mM with the zinc nitrate at a constant concentration of 100 mM. f-j) SEM images of the cross-linked microspheres (f-completely collapsed, g-h partially collapsed due to the air drying before imaging) before and i-j) after the immobilization of ZIF-8 (100 mM zinc nitrate, 400 mM 2-MeIM). k) Representative SEM image and corresponding elemental mapping (Zn, N, and C) of the ZIF-8 immobilized microspheres. l-m) CLSM images of the l) microspheres immobilizing ZIF-8 in suspension and the corresponding m) HIPEs formed after centrifugation, showing the aqueous phase stained green with FITC-BSA.

Immobilization of MOFs. After confirming the successful cross-linking of the CNF-BSA microspheres, our next step was to monitor the formation of the MOF-microsphere composites.

The loading of ZIF-8 can be tuned by controlling the concentration of 2-MeIM (40–800 mM) at a constant concentration of zinc nitrate (100 mM). Transmission electron microscopy (TEM) imaging (Figure 2a-e) reveals that more ZIF-8 nanoparticles formed around the microspheres with increasing concentration of 2-MeIM. At 400 and 800 mM, we can clearly visualize a core-shell structure with a ZIF-8 shell thickness that ranges from 80 to 125 nm (Figure 2d-e). From scanning electron microscopy (SEM), regardless of the completely or partially collapsed state, the bare microspheres exhibited a hollow structure with cross-linked shells featuring a fibrous network (Figure 2f-h). After immobilization of ZIF-8, the microspheres retained their good dispersion (Figure 2i), which is consistent with the sharp single diameter peak from the dynamic light scattering analysis (Figure S8). Higher magnification (Figure 2j) of a ruptured microsphere demonstrated a pollen-like hollow architecture, with abundant individual ZIF-8 nanoparticles (12–30 nm in size) well confined on the shells. We further verified the uniform distribution of the ZIF-8 nanoparticles on the shells by energy dispersive X-ray (EDX) elemental mapping of the microspheres (Figure 2k).

We then centrifuged the MOF-microsphere suspension to form a self-supporting HIPE layer on top of the aqueous phase. This HIPE possessed a solid viscoelastic gel texture (Figure S9) with an internal oil volume fraction of ~86.3%. Note that whatever the MOF precursor concentrations, all the HIPEs were stable without any oiling off (Figure S10a), in sharp contrast to the conventional methods using only small amounts of MOFs (< 20 wt%) in order to avoid phase inversion. To characterize the morphology of the HIPEs, we doped fluorescence-labeled BSA (FITC-BSA) into the bulk BSA solution to stain the aqueous phase.[28] Confocal laser scanning microscopy (CLSM) (Figure 2l-m) and optical microscopy (Figure S10b) images clearly demonstrated the typical HIPE

structure, wherein all the microspheres were tightly packed and deformed into polygonal shapes, yet without coalescing.

We then freeze-dried the HIPEs to prepare the porous foam. Using a direct weighing method,[21] we calculated the mass fractions of the ZIF-8 in the foams to be 21, 39, 58, 72, and 86 wt%, corresponding to the 2-MeIM concentrations of 40, 120, 200, 400, and 800 mM, respectively (Figure S11). These foams also possessed low density that ranged from 7.9–38.5 mg/cm^3. With respect to the morphology, the pure CNF-BSA foam exhibited a 3D-ordered arrangement of interconnecting macrovoids with transport pores (Figure S4). Each void was separated by thick CNF-BSA "walls" and possessed a spiderweb-like nanofibrous network derived from the CNF-BSA cross-linking. Additionally, this unique hierarchical architecture was preserved after ZIF-8 loading, yet both macrovoids and network became more packed (Figure 3a). This is likely because immobilization of the ZIF-8 helps retain the cross-linked network against freeze-drying. Tuning the loading contents of ZIF-8 affected the hierarchical structure of the foam. At 72 wt% ZIF-8, the pore walls became much thinner, and the network was quite compact but fully open, with a transport pore size of 5–20 nm. More importantly, we can clearly see numerous ZIF-8 nanoparticles well dispersed on the fibrous network, the majority of which remained separated from each other (Figure 3b). Further increasing the ZIF-8 loading to 86 wt% led to a partially closed cellular structure with less transport pores, probably due to the close packing of excessive ZIF-8 nanoparticles.

We further tested the meso-macroporosity of the foams using the Brunauer, Emmett, and Teller (BET) method. The N_2 adsorption-desorption isotherms (Figure 3c) displayed a dramatic "tailing" and hysteresis loop at high relative pressures, which can be attributed to the condensation of nitrogen occurring within the macropores of the HIPE polymeric support.[29] The BET surface area

of the foam was proportional to the ZIF-8 loading content, ranging from 79.3 m^2/g (CNF-BSA foam, no ZIF-8) to 227.8 m^2/g (86 wt% ZIF-8 loading). We also verified the mesopore size distribution in the range of 2–40 nm calculated from the Barret-Johner-Halenda (BJH) method (Figure S12).

Again, we used EDX elemental mapping (Figure S13) to demonstrate the homogeneous distribution of ZIF-8 throughout the foams. Powder X-ray diffraction (PXRD) (Figure S14) confirmed the formation of crystalline ZIF-8, showing the characteristic diffraction peaks at 2θ of 7.4° (110), 10.4° (200), 12.8° (211), 16.5° (310), and 18.0° (222).[21] We note this *in situ* synthesis could be extended to other biomacromolecules and MOFs. For example, we also successfully synthesized ZIF-8 nanoparticles within supports composed of CNF-casein, CNF-whey protein isolate, CNF-pea protein, CNF-gelatin, and κ-carrageenan-pectin (Figure S15). Other MOF materials, such as Hong Kong University of Science and Technology-1 (HKUST-1) (Figure S16) and zeolitic imidazolate framework-67 (ZIF-67) (Figure S17), can also be immobilized in the foams using this strategy.

10.1002/anie.201916211

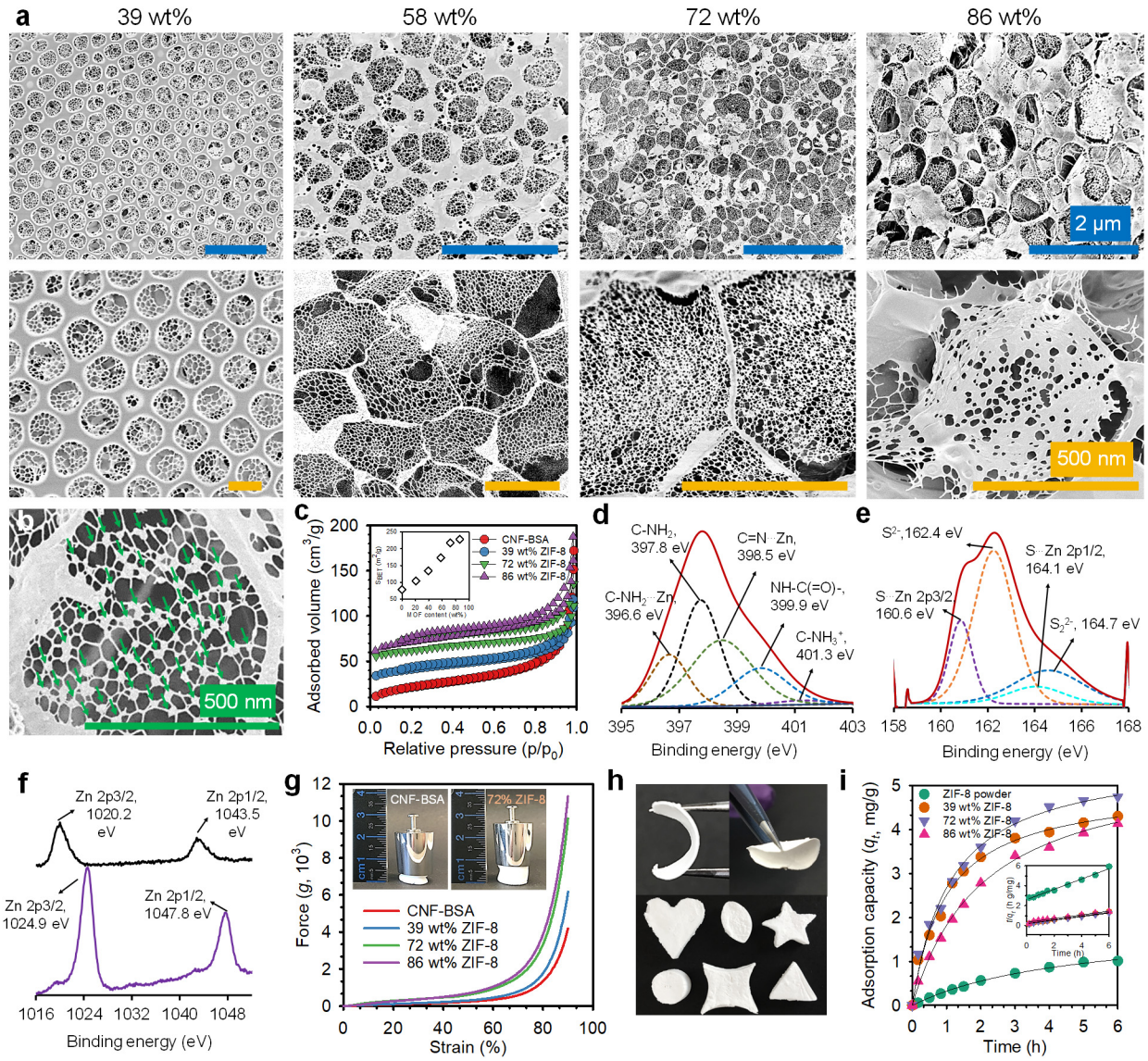

Figure 3. Characterization of the ZIF-8 monolithic foam. a) SEM images of foams loaded with different contents of ZIF-8 (0–86 wt%). b) High magnification of the 58 wt% ZIF-8 foam, the arrows point to the individual ZIF-8 nanoparticles that are uniformly distributed on the fibrous network. c) N_2 adsorption-desorption isotherms. The inset is the dependence of the BET surface area on the ZIF-8 content. d-f) High-resolution XPS spectra of the ZIF-8 foam in the regions of the d) N 1s, e) S 2p, and f) Zn spectra (the upper curve is the pure ZIF-8 bulk powder, the bottom curve is the ZIF-8 foam). g) Compressive stress-strain curves of the foams with various ZIF-8 loadings (39, 72, and 86 wt%), along with the CNF-BSA control. The inset shows the pressing test

with a 30 g weight. h) Processability of the ZIF-8 foam compressed into a thin film that can tolerate bending, and molding to different shapes. i) Time-dependence adsorption capacity of the ZIF-8 foams (normalized to ZIF-8 mass) for Rhodamine B. The inset is the pseudo-second-order kinetic curve.

We next characterized the molecular interactions between the ZIF-8 and CNF-BSA support by high-resolution XPS spectra (Figure 3d-f). After immobilizing ZIF-8, new peaks were observed in the foam at 396.6 eV in the N 1s spectra, and 160.9 eV and 164.7 eV in the S 2p spectra. This suggested the strong interactions of the amine electron pair (from CNF-BSA) and sulfur sites (from BSA) with the accessible Lewis acid sites of the MOFs.[30,31] Furthermore, the peaks at 1021.3 eV and 1044.5 eV, corresponding to the 2p3/2 and 2p1/2 core levels of divalent Zn ions, shifted to 1020 eV and 1043.5 eV, respectively. These lower binding energies implied that the chemical environment of the Zn ions in ZIF-8 were occupied by sulfur and amine groups (S···Zn and C-NH_2···Zn). Similar changes in the chemical signature can also be found in the carbonyl-amide region of the ATR-FTIR spectra and the intrinsic fluorescence quenching of BSA (Figure S18-19). We believe that these strong bonds gave rise to the well-confined growth of ZIF-8 nanoparticles on the microspheres (Figure 2j), and the subsequent tight immobilization in the foam. The latter could minimize the loss and leaching of ZIF-8 during use, which we demonstrated by the observation of hardly any FTIR signal of ZIF-8 released from the foam into water after 2 months of soaking (Figure S20).

Additionally, the strong interactions of the ZIF-8 with the CNF-BSA support provided higher mechanical robustness to the foam. Under compression at 80% strain, the compressive force of the ZIF-8 foam (72 wt%) was 2.47-fold higher than that of the pure CNF-BSA foam (Figure 3g). This was also visualized from a weight pressing test, where the ZIF-8 foam lost less shape than the

CNF-BSA control under a 30 g weight (inset in Figure 3g). The enhanced mechanical stability was consistent with the higher viscoelasticity in the corresponding HIPE form (Figure S9). Given this excellent mechanical stability, the ZIF-8 foam can be formed into task-specific shapes or compressed into a thin film that can even tolerate bending (Figure 3h).

Below we evaluated the performance of MOFs after loading into the foams. First, the potential of these foams as an adsorbent were tested. The ZIF-8 bulk powder, CNF-BSA foam, and ZIF-8 foams (with MOF loadings of 39, 72, and 86 wt%) were soaked in 10 mL of an aqueous solution containing Rhodamine B (13 mg/L). We observed that after adsorbing the dye, the color of the ZIF-8 foam changed from white to red, while the solution became colorless (Figure S21). In the case of the 72 wt% ZIF-8 foam, its equilibrium absorption capacity (q_e) and adsorption rate (k_2) were 2.9- and 2.0-times higher than those of the ZIF-8 bulk powders, respectively (Figure 3i and Table S2). We also characterized the superior adsorption capacity of the ZIF-8 foam using other organic dyes, including methyl blue, orange G, methyl orange, and Rhodamine 6G (Figure S22 and Table S3).

Next, the ZIF-8 foam can also act as a more effective catalyst compared to its powder form. For example, the presence of ZIF-8 in the foam significantly activates peroxymonosulfate (PMS) to quickly degrade dyes in solution (Figure S23-24, Table S4). When using the 72 wt% ZIF-8 loading, the foam showed the highest kinetic rate constant (k) (0.91 h^{-1}), which was significantly higher than those of PMS alone (0.17 h^{-1}) and PMS with the ZIF-8 bulk powder (0.29 h^{-1}). Both the prominent absorption and catalytic capacities of the foams can be attributed to the enhanced accessibility of the MOF meso-macropores through the HIPE hierarchical macropores. This conclusion was supported by the decreased adsorption/catalytic rates of the 86 wt% ZIF-8 foam due to its lower accessibility as a result of its partial closed-cell structure. Note that these foams

10.1002/anie.201916211

were stable during these adsorption and PMS oxidation measurements, without leaching of ZIF-8 nanoparticles or structural change observed (Figure S21, S23).

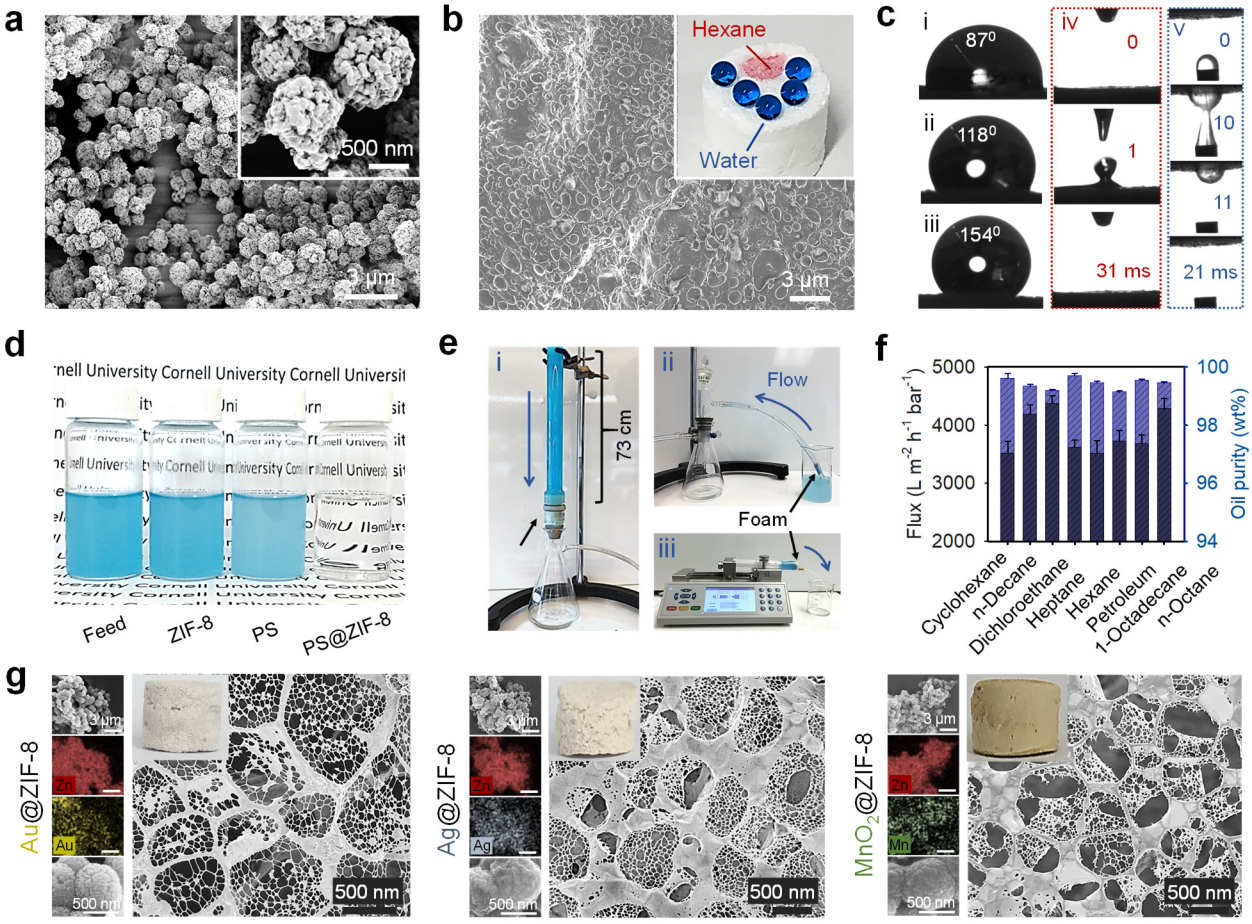

Figure 4. Functionalization of the ZIF-8 foam: superhydrophobic PS@ZIF-8 and metal/metal oxide@ZIF-8 composite foams. a) SEM images of the PS@ZIF-8 microspheres. b) SEM images of the PS@ZIF-8 foam. Inset shows the water and hexane droplets deposited on the PS@ZIF-8 foam (right panel). c) Contact angle measurements: water droplet on the (i) ZIF-8 foam, (ii) PS foam, and (iii) PS@ZIF-8 foam in air; (iv) time dependence of the hexane contact angles on the PS@ZIF-8 foam in air; (v) dynamic underwater contact test showing quick hexane adsorption by the PS@ZIF-8 foam under water. d) Photograph of the water-in-hexane emulsion before and after separation using the ZIF-8 foam, PS foam, and PS@ZIF-8 foam. e) The use of the flexible foam

in different home-made filtration units, composed of a (i) glass tube, (ii) flexible pipe, and (iii) syringe pump. f) Flux and oil purity in the filtrate after passing through the PS@ZIF-8 foam for a variety of water-in-oil emulsions. To obtain color contrast, dyed water (stained with methylene blue) and oil (stained with Sudan IV) were used in (b, d, e) and (b), respectively. g) SEM images of the metal/metal oxie@ZIF-8 composite foams. In each figure group, the left shows the microspheres immobilizing the metal/metal oxide@ZIF-8, and the corresponding elemental mapping.

Functionalization of MOF Foam. Another advantage of our strategy for the independent synthesis of the microspheres and HIPE is its ability to easily impart additional functionality to the framework. For example, we can pre-incorporate a hydrophobic polymer (e.g., polystyrene (PS)) by dissolving it in the oil phase prior to synthesis, resulting in PS@ZIF-8 microspheres that had rather rough surfaces (Figure 4a). The incorporation of PS enhanced the foam robustness under compression but did not affect the immobilization of ZIF-8 with a mesopore size of 2–50 nm (Figure S25). Interestingly, the PS@ZIF-8 foam possessed mainly closed-cell voids (Figure 4b), in contrast to the open-cell structure of the pristine ZIF-8 foam (Figure 3a) and PS foam (Figure S26). Such closed-cell mesoporous structure together with the hydrophobicity of PS could significantly increase the water entry pressure into the foam. Indeed, we found that the PS@ZIF-8 foam can float on the surface of water and did not uptake any water even when immersed by an external force (Figure S27). Water can also bead up on the surface of the foam, in contrast to the immediate adsorption of hexane (Figure 4b, inset). We also directly demonstrated the superhydrophobicity of the PS@ZIF-8 foam by its water contact angle of 154° in air, which is much higher than that of the pristine ZIF-8 foam (87°) or PS foam (118°) (Figure 4c, i-iii). In

contrast to water, a 2 μL droplet of hexane immediately penetrated through the PS@ZIF-8 foam in both air and water within 31 ms and 21 ms, respectively (Figure 4c, iv-v).

We hypothesized that the excellent water-nonwetting and superoleophilicity of the PS@ZIF-8 foam would endow it with the capability for oil/water separation. To confirm this, we placed the ZIF-8, PS, and PS@ZIF-8 foams into a 3 mL Luer-Lok tip syringe to filter a water-in-hexane emulsion by hand-pressing (Figure 4d and Figure S28a). The original emulsion was blue (water dyed with methylene blue) and opaque. After filtration by the ZIF-8 and PS foams, the emulsion only turned partially clear. In contrast, when PS@ZIF-8 was used, the emulsion turned colorless and transparent containing exclusively tiny water droplets < 2 nm (Figure S28b-d).

More importantly, the flexibility of the PS@ZIF-8 foam allowed us to fix it in various large-scale filtration units for continuous separation, suggesting high potential for industry applications. The units included a glass tube, flexible pipe, and syringe pump (Figure 4e, Movie S1-3). Through a conventional glass tube unit (height of 73 cm), we can use 2.8 g of PS@ZIF-8 foam to effectively separate at least 250 mL of water-in-hexane emulsion (oil purity of 99.4 wt% in filtrate) in one cycle (Figure S29). This excellent separation performance was also demonstrated by a series of different water-in-oil emulsions and corresponding fluxes. All emulsions were successfully separated with oil purities of 99.2–99.7 wt% (Figure 4f and Figure S30) at high fluxes ranging from 3500–4400 L m^{-2} h^{-1} bar^{-1}, which are around two orders of magnitude higher than commercial filtration membranes.[32,33] After simply washing with ethanol and water, the foam can also be repeatedly used for at least five times without obvious decrease of oil purity or flux in every separation cycle (Figure S31). The antifouling performance of the PS@ZIF-8 foam was also characterized by its high antimicrobial activity (Figure S32). Additionally, in a batch study, we used a piece of PS@ZIF-8 foam to remove hexane floating in water and underwater dichloroethane

within several seconds (Figure S33). In addition to the oil/water separation, the superhydrophobic nature of the foam also endows it with various attractive features, including self-cleaning, underoil water repellency, blood repellency, and anti-icing properties (Figure S34). We also note that at harsh conditions, such as strong acid, base, and ionic strength, the PS@ZIF-8 foam still demonstrated strong resistance (Figure S35-36).

Finally, we evaluated the potential of this strategy for synthesizing MOF-based heterostructures. For a proof-of-concept, we added three types of metal ions, including $HAuCl_4$, $AgNO_3$, and $MnCl_2$, into the suspension of CNF-BSA microspheres, followed by adjusting the pH to 11–12 and addition of ZIF-8 precursor solution (see Figure S37 for more details). SEM images show the good dispersion of these metal/metal oxide@ZIF-8 microspheres, whose surfaces were composed of nanoclusters with a size of 30–70 nm (Figure 4g). EDX elemental mapping further confirmed the successful pre-confinement of these metal materials and subsequent growth of ZIF-8. After a centrifugation/freeze-drying protocol, we obtained the uniform and flexible Au@ZIF-8, Ag@ZIF-8, and MnO_2@ZIF-8 composite foams. We observed that the supernatant was transparent and colorless, implying that the metal/metal oxide@ZIF-8 materials were effectively incorporated in the HIPEs. PXRD of these foams demonstrated the formation of crystalline ZIF-8 (Figure S38). All the foams maintained the spiderweb-like hierarchical structures, with metal/metal oxide@ZIF-8 composites dispersed around the walls (Figure 4g). The successful integration of metal/metal oxide materials could impart additional functionalities to the MOF-based platforms for application in catalysis or sensing.

Conclusion

We have synthesized a unique meso-macroporous MOF platform by a HIPE templating strategy, which is applicable to a broad range of MOFs and biopolymers, and the fabrication process is

general, facile, environmentally friendly, and suitable for large-scale production (room temperature synthesis involving traditional lab equipment). The findings of this study provide several advances to the field of MOF macroscopic materials, including good dispersion of MOF nanoparticles at high loadings, a well-defined hierarchical porous system, independent control over the organization of the MOFs and the interconnecting macroporous network of the support, and simple fabrication of MOF composites by integrating other functional materials. The resulting spiderweb-like porous system enables high surface area, and pore accessibility, and thus superior adsorption and catalytic capacities. Due to the ability to fine tune the properties of this hierarchical platform, further exploration of our strategy features the potential for designing more complex structural and compositional combinations, providing strong potential for MOF-based hybrid materials science in real-world applications, such as separations, catalysis, tissue engineering, controlled drug delivery, biology, and pharmaceuticals.

Supporting Information

Supporting Information is available from the Wiley Online Library or from the author.

Acknowledgements

We thank the Cornell Center for Materials Research (CCMR) for use of their facilities. CCMR facilities are supported by the National Science Foundation under award number DMR-1719875.

References

[1] G. Liu, V. Chernikova, Y. Liu, K. Zhang, Y. Belmabkhout, O. Shekhah, C. Zhang, S. Yi, M. Eddaoudi, W. J. Koros, *Nat. Mater.* **2018**, *17*, 283-289.

[2] G. Lu, S. Li, Z. Guo, O. K. Farha, B. G. Hauser, X. Qi, Y. Wang, X. Wang, S. Han, X. Liu, et al., *Nat. Chem.* **2012**, *4*, 310-316.

[3] H. Zheng, Y. Zhang, L. Liu, W. Wan, P. Guo, A. M. Nyström, X. Zou, *J. Am. Chem. Soc.*

2016, *138*, 962-968.

[4] J. Baek, B. Rungtaweevoranit, X. Pei, M. Park, S. C. Fakra, Y. S. Liu, R. Matheu, S. A. Alshmimri, S. Alshehri, C. A. Trickett, et al., *J. Am. Chem. Soc.* **2018**, *140*, 18208-18216.

[5] H. Kim, S. Yang, S. R. Rao, S. Narayanan, E. A. Kapustin, H. Furukawa, A. S. Umans, O. M. Yaghi, E. N. Wang, *Science.* **2017**, *356*, 430-434.

[6] Y. Peng, V. Krungleviciute, I. Eryazici, J. T. Hupp, O. K. Farha, T. Yildirim, *J. Am. Chem. Soc.* **2013**, *35*, 11887-11894.

[7] J. Dechnik, J. Gascon, C. J. Doonan, C. Janiak, C. J. Sumby, *Angew. Chemie - Int. Ed.* **2017**, *56*, 9292-9310.

[8] K. Xie, Q. Fu, P. A. Webley, G. G. Qiao, *Angew. Chemie - Int. Ed.* **2018**, *57*, 8597-8602.

[9] T. Tian, Z. Zeng, D. Vulpe, M. E. Casco, G. Divitini, P. A. Midgley, J. Silvestre-Albero, J. C. Tan, P. Z. Moghadam, D. Fairen-Jimenez, *Nat. Mater.* **2018**, *17*, 174-179.

[10] L. Li, S. Xiang, S. Cao, J. Zhang, G. Ouyang, L. Chen, C. Y. Su, *Nat. Commun.* **2013**, 4, 1774.

[11] K. Jayaramulu, F. Geyer, M. Petr, R. Zboril, D. Vollmer, R. A. Fischer, *Adv. Mater.* **2017**, 29, 1605307.

[12] S. S. Park, C. H. Hendon, A. J. Fielding, A. Walsh, M. O'Keeffe, M. Dincă, *J. Am. Chem. Soc.* **2017**, *139*, 3619-3622.

[13] L. Wang, X. Feng, L. Ren, Q. Piao, J. Zhong, Y. Wang, H. Li, Y. Chen, B. Wang, *J. Am. Chem. Soc.* **2015**, *137*, 4920-4923.

[14] S. R. Ahrenholtz, C. C. Epley, A. J. Morris, *J. Am. Chem. Soc.* **2014**, *136*, 2464-2472.

[15] J. Gu, H. Fan, C. Li, J. Caro, H. Meng, *Angew. Chemie - Int. Ed.* **2019**, *131*, 5351-5355.

[16] H. Zhu, X. Yang, E. D. Cranston, S. Zhu, *Adv. Mater.* **2016**, *28*, 7652-7657.

[17] Y. Chen, X. Huang, S. Zhang, S. Li, S. Cao, X. Pei, J. Zhou, X. Feng, B. Wang, *J. Am. Chem. Soc.* **2016**, *138*, 10810-10813.

[18] D. Kim, D. W. Kim, O. Buyukcakir, M. Kim, K. Polychronopoulou, A. Coskun, *Adv. Funct. Mater.* **2017**, *27*, 1700706.

[19] Y. Sun, F. Yang, Q. Wei, N. Wang, X. Qin, S. Zhang, B. Wang, Z. Nie, S. Ji, H. Yan, et al., *Adv. Mater.* **2016**, *28*, 2374-2381.

[20] Y. Mao, J. Li, W. Cao, Y. Ying, P. Hu, Y. Liu, L. Sun, H. Wang, C. Jin, X. Peng, *Nat. Commun.* **2014**, *5*, 5532.

[21] L. Zhu, L. Zong, X. Wu, M. Li, H. Wang, J. You, C. Li, *ACS Nano* **2018**, *12*, 4462-4468.

[22] W. Yang, Y. Han, C. Li, L. Zhu, L. Shi, W. Tang, J. Wang, T. Yue, Z. Li, *Chem. Eng. J.* **2019**, *375*, 122076.

[23] M. G. Schwab, I. Senkovska, M. Rose, M. Koch, J. Pahnke, G. Jonschker, S. Kaskel, *Adv. Eng. Mater.* **2008**, 10.

[24] M. Arshadi, M. Azizi, H. Soozandeh, C. Tan, S. M. Davachi, A. Abbaspourrad, *J. Mater. Chem. A* **2019**, *7*, 26456-26468.

[25] K. Landfester, *Angew. Chemie - Int. Ed.* **2009**, *48*, 4488–4508.

[26] C. Tan, M. Arshadi, M. C. Lee, M. Godec, M. Azizi, B. Yan, H. Eskandarloo, T. W. Deisenroth, R. H. Darji, T. Van Pho, et al., *ACS Nano* **2019**, *13*, 9016-9027.

[27] C. Tan, M. C. Lee, S. Pajoumshariati, A. Abbaspourrad, *ACS Sustain. Chem. Eng.* **2018**, *6*, 14374-14382.

[28] C. Tan, M. C. Lee, A. Abbaspourrad, *ACS Sustain. Chem. Eng.* **2018**, *6*, 16657-16664.

[29] Y. Yang, L. Cao, J. Li, Y. Dong, J. Wang, *Macromol. Mater. Eng.* **2018**, *303*, 1800426.

[30] Y. Zhao, Y. Dong, F. Lu, C. Ju, L. Liu, J. Zhang, B. Zhang, Y. Feng, *J. Mater. Chem. A*

2017, 5, 15380-15389.

[31] W. Li, Y. Zhang, P. Su, Z. Xu, G. Zhang, C. Shen, Q. Meng, *J. Mater. Chem. A* **2016**, *4*, 18747-18752.

[32] G. Gutiérrez, A. Lobo, J. M. Benito, J. Coca, C. Pazos, *J. Hazard. Mater.* **2011**, *2*, 1569-1574.

[33] B. Chakrabarty, A. K. Ghoshal, M. K. Purkait, *J. Memb. Sci.* **2008**, *325*, 427-437.

10.1002/anie.201916211

Table of Contents

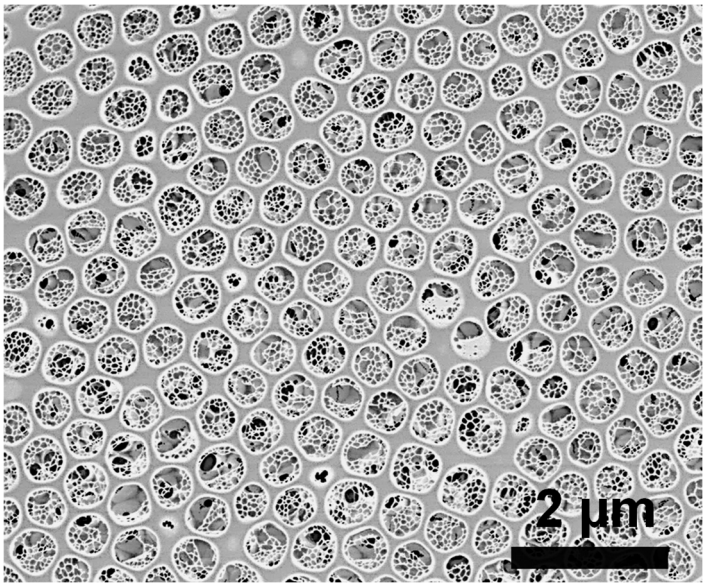

We present a general strategy for precise control over the properties of both the hierarchical support and MOFs, enabling the good dispersion of individual MOF nanoparticles on a spiderweb-like network within each macrovoid even at high loadings.